J. Eng. Technol. Sci., Vol. 54, No. 2, 2022, 220204

Experimental and Numerical Analysis of Carbon/Epoxy Composite Plate Subject to Low-Velocity Impact

Muhamad Giri Suada[1,*], Hendri Syamsudin[1] & Haroen Romadon.[2]

[1]Lightweight Structure Research Group, Faculty of Mechanical and Aerospace Engineering, Institut Teknologi Bandung, Jalan Ganesa No. 10, Bandung 40132, Indonesia
[2]Direktorat Teknologi, PT Dirgantara Indonesia, Jalan Pajajaran 154, Bandung 40174, Indonesia
*E-mail: mgsuada@gmail.com

Highlights:

- The Benzeggagh-Kenane fracture criterion and the Hashim-Rotem damage mechanism proved to be capable of perfectly predicting surface damage and projected delamination of the composite material subjected to low-velocity impact.
- Mass model selection is suspected to be the reason for slight differences in mimicking the dynamic response.
- Selection of a Kirchoff based shell element contributed to poor bending stiffness modeling of the composite plate, leading to a significant difference in predicting the quantity of absorbed energy.

Abstract. The present work compared experimental and finite element analysis on the low-velocity impact response of a carbon/epoxy composite plate. Finite element analysis was based on the utilization of cohesive zone elements with the Benzeggagh-Kenane fracture criterion to predict the initiation and propagation of delamination. A Kirchhoff based formulation of a continuum shell element was used to model the stiffness of each lamina and the Hashim-Rotem damage mechanism to predict damages in every lamina. Five specimens of a 16-layer uni-directional carbon/epoxy composite plate with fiber orientation $[+45°/90°/-45°/0°/+45°/90°/-45°/0°]_s$ were subjected to low-velocity impact with a single energy value of 2.75 Joule/mm. The experimental results were then compared to the finite element results. Good agreement was achieved for the size and shape of the total projected delamination and visual damage to the top and bottom surface in the form of matrix and fiber failure. Slight differences were found for the dynamic response in the impact force history. Furthermore, a significant difference was found for the quantity of absorbed energy.

Keywords: *barely visible impact damage; carbon composite laminate; delamination; finite element; low-velocity impact.*

Received November 11th, 2020, 1st Revision April 2nd, 2021, 2nd Revision July 11th, 2021, Accepted for publication September 29th, 2021.
 ISSN: 2337-5779, DOI: 10.5614/j.eng.technol.sci.2022.54.2.4

1 Introduction

Low-velocity impact on composite laminate structures has attracted attention from many researchers, among others [1-3], and [4]. The low-velocity impact on composite material creates barely visible impact damage (BVID). Unfortunately, such barely visible impact damage can create invisible damage in the form of delamination [5]. Gonzalez, *et al.* [6] studied the effects of ply clustering on polymer-based laminated composite plates subjected to drop-weight impact loading. They observed the impact behavior and aimed to find the impact damage threshold for significantly reducing the structural stiffness and compression strength due to delamination. They conducted an experimental test on Hexply AS4/8552 carbon epoxy unidirectional prepreg with different stacking sequences, i.e., $[(45°/0°/-45°/90°)4]_s$, $[(45°_2/0°_2/-45°_2/90°_2)2]_s$, and $[(45°_4/0°_4/-45°_4/90°_4)]_s$. They found that the most critical damage of drop weight impact was delamination, where each lay-up had a different dynamic response and form of delamination.

The typical damage modes after low-velocity impact are illustrated in Figure 1 [6]:

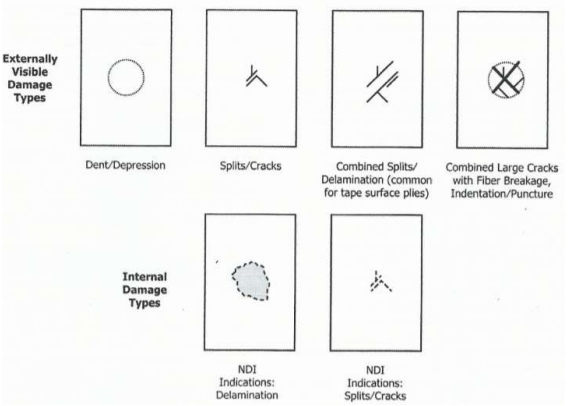

Figure 1 Types of composite plate damage [6].

The present paper delivers the results of experimental and numerical approaches to the low-velocity impact analysis of a 16-layer uni-directional (UD) carbon/epoxy composite plate with fiber orientation $[+45°90°/-45°/+45°/90°/-45°/0°]_s$. The numerical-approach utilized a cohesive zone element and the Benzeggagh-Kenane fracture criterion to predict the initiation and propagation of delamination, a Kirchhoff based formulation of a continuum shell element to model the stiffness of each lamina, and the Hashim-Rotem damage mechanism to predict damage to every lamina. The ABAQUS finite element software was

used for the whole explicit numerical analysis. The finite element result was then verified with the experimental results. The verification was executed by comparing the size of the total projected delamination, visual damage on the top and bottom surface in the form of matrix and fiber failure, absorbed energy, force-displacement history, dynamics response in the form of the impact force history, and the impact force threshold. The accuracy of predicting permanent damage after impact in the form of delamination and visible surface damage was the main interest of the present work.

2 Testing Method

The test specimen was made of Hexply AS4/8552 16-layer UD carbon/epoxy composite plate with fiber orientation $[+45°/90°/-45°/+45°/90°/-45°/0°]_s$. The specimen size and testing methods followed ASTM D7136 [7]. Five specimens were made and tested under a single value of 2.75 J/mm energy impact. The impact energy was dictated such that the damage created was within the classification of BVID as defined in Ref. [8]. The thickness of the specimen was between 3.8 and 3.9 mm, with an average value of 3.84 mm. Low-velocity impact testing was carried out using an INSTRON 9350 impact drop weight impact testing machine, in compliance with ASTM D7136.

3 Finite Element Model and Material Properties

Mesh sensitivity analysis in the case of low-velocity impact determines the effect of element size on the results of low-velocity impact simulations, i.e., threshold force, peak force, and computational efficiency in terms of time needed for numerical simulation. The authors in [9] conducted a finite element analysis using the configuration and element size suggested in Ref. [10]. Figure 2 shows the mesh used in this analysis. Each lamina was modeled as a single-layer continuum shell meshed with SC8R reduced integration elements and a cohesive zone interface model was placed in between the lamina and meshed with a single layer COH3D8 cohesive element.

The SC8R continuum shell element was based on the Kirchhoff plate bending theory. This theory neglects any shear deformation. ABAQUS provides only Kirchhoff based shell elements [11]. The element's size was chosen following Song [10]. Song suggested that the size of the cohesive element should be fine enough to capture the high gradient stress fields near the tip of delamination. Song states that the maximum element length (Le) to achieve this is given by $Le = E_i G_{ci}/(Ne\, S_i^2)$, $Ne \geqq 3$, $i = t,n,s$. The value of S_i can be adjusted such that coarser meshes will start to fail simultaneously at more refined meshes. By keeping G_c constant, the energy dissipation of the elements is preserved. This is achieved by

rearranging the previous equation into $S_i = (E_i \ G_{ci}/[Ne \ Le])^{0.5}$. The recommendations from [9] and [12] and careful calculations led to a size of 1.25 mm (length) x 1.25 mm (wide) x 0.23 mm (thick) for the SC8R elements and 1.25 mm (length) x 1.25 mm (wide) x 0.006 mm (thick) for the COH3D3 elements. The smallest element was suggested to be placed in the possible delaminated area. A coarser mesh was placed outside the damage zone to minimize the number of elements. In the present study, the total number of elements reached up to 180,000 elements.

No-clustering mesh modeling was used in the present model, as suggested by Ref. [13]. The base plate was modeled as a discrete rigid surface meshed with R3D4 elements and the pins were modeled as analytical rigid body cylinders. Further reading about the elements can be found in Ref. [14]. The fixture was placed in contact with the laminates with no compressive force applied to the laminate and both translation and rotation were constrained in all directions for the fixture. The impactor was modeled as an analytical rigid body sphere with 0.01 mm distance from the top of the laminate surface with an initial velocity of 2.05 m/s and placed in the middle of the sphere so the impact energy reached 10.5 Joule.

Translation was only permitted in the transverse axis to the laminate surface. All other translations were constrained. The effect of gravitational acceleration was neglected to make the energy analysis easier. The contact between fixtures–laminate, impactor–laminate, and cluster–cluster was defined by the general contact option.

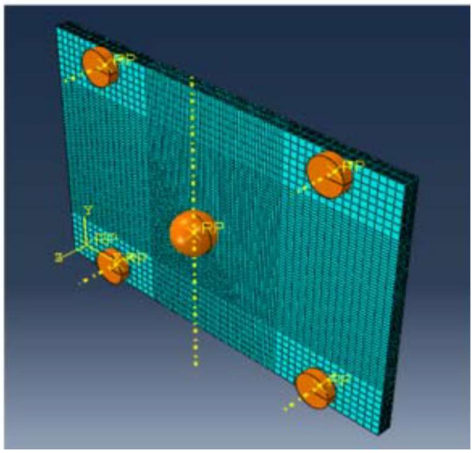

Figure 2 Finite element model of the 16-layer $[+45°/90°/-45°/0°/+45°/90°\ 45°/0°]_s$ carbon composite plate subjected to low-velocity impact.

The value of transverse shear stiffness (G_{23}) was obtained assuming that the transverse shear fiber cross-section isotropic and $\mu_{23} = \mu_{12}$ such that $G_{23} = E_{22}/2(1+\mu_{12})$. The fracture energies (G_c) were taken from Gonzales [4]. The friction coefficient μ was taken as 0.6, as suggested in [15]. The properties of Hexply AS4/8552 and the cohesive zone interface as taken from [5] are as follows:

Table 1 Material properties of Hexply AS4/8552.

Properties	Values
Fiber direction stiffness, E_{11} (MPa)	131610
Transverse fiber direction stiffness, E_{22} (MPa)	9238.
In-plane shear stiffness, G_{12} (MPa)	4826.
Transverse shear stiffness, G_{13} (MPa)	3548
Longitudinal shear stiffness, G_{13} (MPa)	4826.
In-plane Poisson's ratio, μ_{12}	0.302
Density (ton/mm^3)	1.59×10^{-9}
Fiber direction tension strength, X_T (MPa)	2063.
Fiber direction compression strength, X_C (MPa)	1484.
Transverse fiber direction tension strength, Y_T (MPa)	63.
Transverse fiber compression tension strength, Y_C(MPa)	267.
In-plane shear strength, S_{12} (MPa)	91.
Transverse shear strength, S_{23} (MPa)	133.
G_{ft} Fracture energy fiber direction in tension (N/mm)	81.5
G_{fc} fiber direction in compression (N/mm)	106.3
G_{mt} transverse fiber direction in tension (N/mm)	0.28
G_{mc} transverse fiber direction in compression (N/mm)	0.79

Table 2 Cohesive zone interface properties.

Properties	Values
Normal stiffness, k_n (MPa/mm)	36955.
Shear stiffness, k_t, and k_s (MPa/mm)	19305.
Maximum normal stress, N_{max} (MPa)	26.26
Maximum shear stress, $S_{max} = T_{max}$ (MPa)	31.89
Normal fracture energy (N/mm)	0.28
Shear fracture energy (N/mm)	0.79
Density, ρ(ton/mm^3)	1.59×10^{-9}
BK mix mode parameter, η	1.45

4 Damage Evolution Model

The damage evolution mechanism was divided into two folds. The first one was for intra-laminar damage and the other one was for inter-laminar damage. In the intra-laminar model, the damage evolution deals with predicting damage initiation and evolution in the lamina in the form of matrix tension/compression

failure, fiber direction tension, and compression failure. The Hashin-Roten damage model mechanism [16] was used in the present numerical analysis. The inter-laminar damage model mechanism deals with the prediction and propagation of delamination in the layer model. A brief description of the damage evolution model is described below.

4.1 Intra-laminar Damage Evolution Model

The failure criteria used for fiber-reinforced composites state four different failure initiations: fiber tension, fiber compression, matrix tension, and matrix compression.

Fiber tension $(\varepsilon_1 > 0)$

$$F_{ft}^2 = \left(\frac{\varepsilon_1}{\varepsilon_{1t}^f}\right)^2 + \left(\frac{\gamma_{12}}{\gamma_{12}^f}\right)^2 + \left(\frac{\gamma_{13}}{\gamma_{13}}\right)^2 \quad (1)$$

Fiber compression $(\varepsilon_1 < 0)$

$$F_{fc}^2 = \left(\frac{\varepsilon_1}{\varepsilon_{1c}^f}\right)^2 \quad (2)$$

Matrix tension $(\varepsilon_2 + \varepsilon_3 > 0)$

$$\mathrm{F}_{mt}^2 = \left(\frac{\varepsilon_2+\varepsilon_3}{\varepsilon_{2t}^f}\right)^2 - \frac{\varepsilon_2\varepsilon_3}{{\gamma_{23}^f}^2} + \left(\frac{\gamma_{12}}{\gamma_{12}^f}\right)^2 + \left(\frac{\gamma_{12}}{\gamma_{12}^f}\right)^2 + \left(\frac{\gamma_{12}}{\gamma_{12}^f}\right)^2 \quad (3)$$

Matrix compression $(\varepsilon_2 + \varepsilon_3 < 0)$

$$F_{mt}^2 = \left[\left(\frac{\varepsilon_{2c}^f}{2\gamma_{23}^f}\right)^2 - 1\right]\left(\frac{\varepsilon_2+\varepsilon_3}{2\tau_{23}^f}\right) + \left(\frac{\varepsilon_2+\varepsilon_3}{2\tau_{23}^f}\right)^2 - \frac{\varepsilon_2\varepsilon_3}{{\tau_{23}^f}^2} + \left(\frac{\gamma_{12}}{\gamma_{12}^f}\right)^2 + \left(\frac{\gamma_{12}}{\gamma_{12}^f}\right)^2 + \left(\frac{\gamma_{12}}{\gamma_{12}^f}\right)^2 \quad (4)$$

Subscripts c and t denote compressive and tensile strain failures and subscript f indicates strain failure. Failure strains are derived from material properties.

$$\varepsilon_{1t}^f = \frac{X_t}{C_{11}} \quad (5) \qquad \varepsilon_{1c}^f = \frac{X_c}{C_{11}} \quad (8)$$

$$\varepsilon_{2t}^f = \frac{Y_t}{C_{22}} \quad (6) \qquad \varepsilon_{2c}^f = \frac{Y_c}{C_{22}} \quad (9)$$

$$\gamma_{ij}^f = \frac{S_{ij}}{G_{ij}} \quad (7) \qquad (i,j=1,2,3)$$

X_t and X_C are the longitudinal tensile and compressive stresses, while Y_t and Y_C are the transverse tensile and compressive stresses, S_{ij} is shear strength in the *i-j* plane. After the material reaches the failure criteria, i.e., when the F index reaches a value of 1, the material properties will experience linear degradation.

Furthermore, the material will experience evolutionary damage with variable damage dM = f (FM). The damage evolution for each failure criterion is:

Fiber tension $(\varepsilon_1 > 0)$

$$d_{ft} = 1 - \left(\frac{1}{F_{ft}} exp\left(-\frac{X_t \varepsilon_{1t}^f L^c (F_{ft}-1)}{G_{ft}}\right)\right) \tag{10}$$

Fiber compression $(\varepsilon_1 < 0)$

$$d_{fc} = 1 - \left(\frac{1}{F_{fc}} exp\left(-\frac{X_c \varepsilon_{1c}^f L^c (F_{fc}-1)}{G_{fc}}\right)\right) \tag{11}$$

Matrix tension $(\varepsilon_2 + \varepsilon_3 > 0)$

$$d_{mt} = 1 - \left(\frac{1}{F_{mt}} exp\left(-\frac{Y_t \varepsilon_{2t}^f L^c (F_{mt}-1)}{G_{mt}}\right)\right) \tag{12}$$

Matrix compression $(\varepsilon_2 + \varepsilon_3 < 0)$

$$d_{mc} = 1 - \left(\frac{1}{F_{mc}} exp\left(-\frac{Y_c \varepsilon_{2c}^f L^c (F_{mc}-1)}{G_{mc}}\right)\right) \tag{13}$$

where L^C is the characteristic length of the cohesive elements, G_{ft}, G_{fc}, G_{mt}, G_{mc} are fracture energies in the direction of the longitudinal tensile, longitudinal compressive, transverse tensile, and transverse compression. The failure behavior of the lamina material in the elastic phase from 0 to A and in the post-elastic phase from A to C is shown in Figure 3.

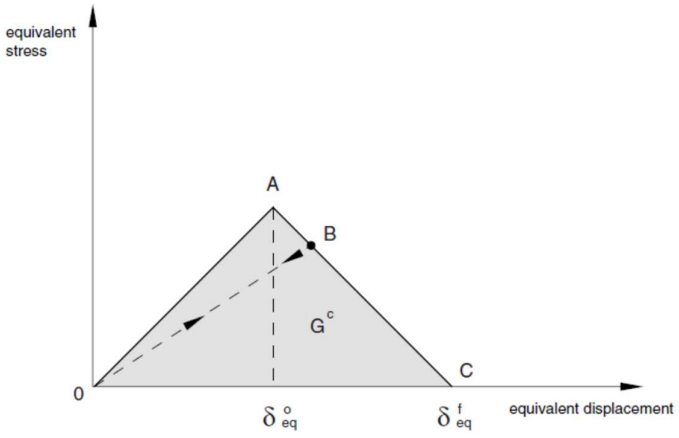

Figure 3 Progressive damage model [16].

The stress-strain vector relationship and the constitutive model with linear degradation are formulated as follows:

$$\sigma = C_d \varepsilon \tag{14}$$

$$C_d = \frac{1}{D} \times \begin{bmatrix} (1 - d_f)E_1 & (1 - d_f)(1 - d_m)\nu_{12}E_{12} & 0 \\ (1 - d_f)(1 - d_m)\nu_{12}E_{12} & (1 - d_m)E_2 & 0 \\ 0 & 0 & (1 - d_s)GD \end{bmatrix} \tag{15}$$

$$D = 1 - (1 - d_f)(1 - d_m)\nu_{12}\nu_{21} \tag{16}$$

with

$d_f = d_{ft}$, $\varepsilon_1 > 0$

$d_f = d_{fc}$, $\varepsilon_1 < 0$

$d_m = d_{mt}$, $\varepsilon_2 + \varepsilon_3 > 0$

$d_m = d_{mc}$, $\varepsilon_2 + \varepsilon_3 < 0$

4.2 Inter-laminar Damage Evolution Model

Inter-laminar damage evolution modeling was conducted using a cohesive zone element. The cohesive zone element controls the traction-reaction on two surfaces that are attached and detaches and is expressed by the displacement of the two surfaces. This concept applies if the stress is dominated by normal stress and plane stress only and stress in the axial direction of the field does not exist. Possible relative displacement is in the normal/peeling and sliding directions. This displacement also includes traction (t_n,t_s,t_t), which shows the bond resistance between the two surfaces. t_n is normal traction and t_s and t_t are two perpendicular shear tractions. The traction separation behavior is stated in:

$$\{t\} = [K]\{\varepsilon\} \tag{17}$$

where $\{\varepsilon\}$ is the relative displacement separation vector (δ_n,δ_s,δ_t in normal and two perpendicular shear directions) and [K] is the cohesive material stiffness matrix. Vector t is the nominal value of traction. The damage initiation in the cohesive zone is assumed to initiate when quadratic interaction involving the nominal stress ratio reaches a value of 1.

$$\left(\frac{t_n}{N_{max}}\right) + \left(\frac{t_s}{S_{max}}\right) + \left(\frac{t_t}{T_{max}}\right) = 1 \tag{18}$$

After the initiation traction failure criteria have been achieved, the component's stiffness experiences softening with a scalar breakdown variable d so that variable

d varies from 0 to 1, with 1 representing material failure, i.e., material stiffness *k* reaches 0. This is illustrated in Figure 4. The total triangle area in Figure 4 is proportional to the critical fracture energy. Therefore, once the fracture condition reaches its critical value, delamination increases.

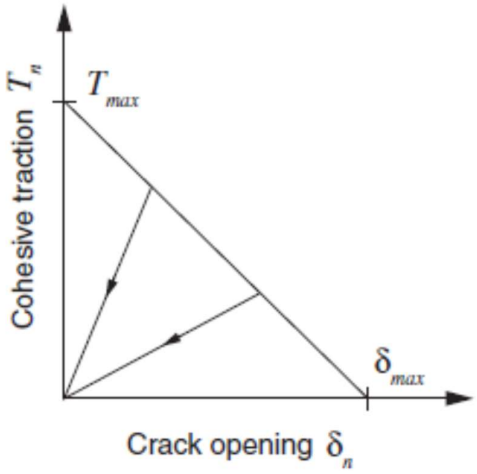

Figure 4 Traction-separation response [17].

For mixed-mode cases, the adopted formulation to control the progress of delamination is the Benzeggagh-Kenane fracture criterion [17]. The proposed formula is $G_S = G_s + G_t$, and $G_T = G_n + G_S$, and η are the material parameters.

$$G_n^c + (G_s^c\ G_n^c)\left(\frac{G_S}{G_T}\right)^{\eta}\ G^c \tag{19}$$

5 Results and Discussion

5.1 Energy Variation During Numerical-Analysis

Observation of the energy distribution during the numerical analysis is essential to see if the artificial energy is relatively high compared to the total energy. Artificial energy is related to hourglass deformation. The accepted artificial energy must be below 5% of the total energy during the numerical iteration, as suggested by Ref. [14]. In the present work, the maximum artificial energy was 0.48 J, compared to the calculated total energy of 10.5 J, which is the only infraction of less than 5%. Therefore the complete numerical analysis result was classified as acceptable without excessive artificial energy disruption. The total energy was 10.5 joule, equal to the impact energy loaded to the plate. As shown

in Figure 5, the internal energy is the absorbed energy, which had a value of 3.7 Joule.

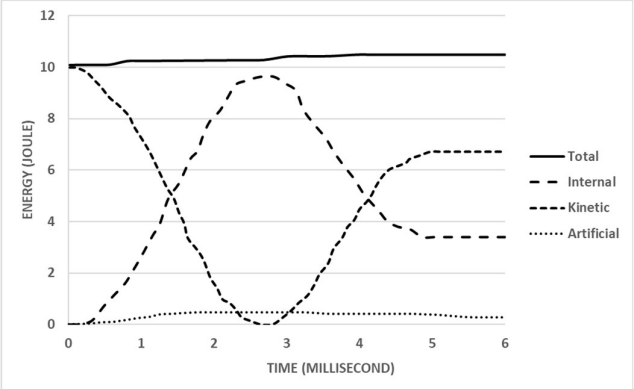

Figure 5 Energy variation during the numerical analysis.

5.2 Force-time History

The Figure 6 shows the average value of the experimental results and the numerical analysis results in the form of a force-time history. From Figure 6, we can see that the peak force difference between the experimental and the numerical analysis results was significantly large. Meanwhile, the threshold force value was closely similar.

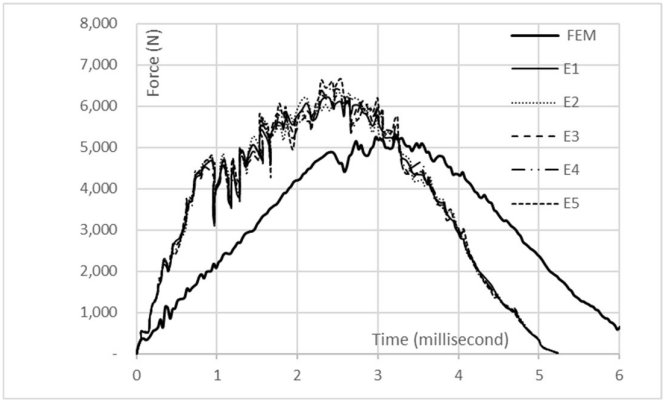

Figure 6 Impact force-time histories during impact. Experiment results (E1-E5) and numerical result (FEM).

The experimental and numerical curves were almost the same, even though the numerical result lagged in time response in the order of 1 millisecond. This indicates that the experimental and the numerical analysis were almost the same dynamically during the impact process. Table 3 below shows both the experimental and the numerical analysis results for the peak and threshold impact force.

Table 3 Peak and threshold impact force.

	Average Experimental (N)	Numerical-FEM (N)	Deviation (%)
Peak Force	6016	5224	-13.1
Threshold Force	4887	4893	0.12

The threshold impact force, according to Ref. [5], is considered the point where delamination starts propagating rapidly and is identified as the first sharp drop of impact force when there is a sudden loss of stiffness.

5.3 Force-displacement History

The following figure shows the average values of the experimental and the numerical analysis results in the form of a force-displacement history:

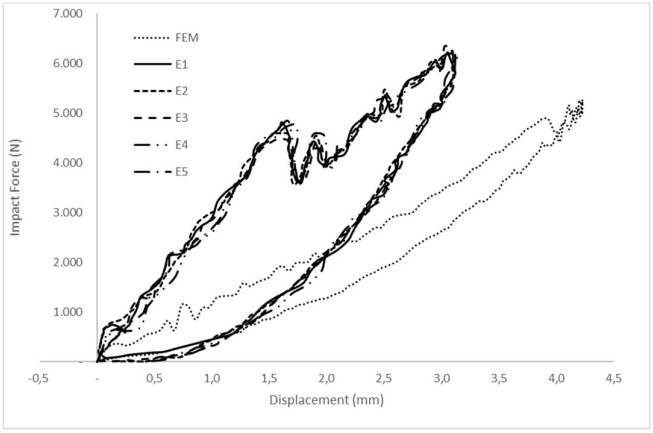

Figure 7 Force-displacement histories during impact for the experimental results (E1-E5) and the numerical result (FEM).

Figure 7 shows the discrepancies between the bending stiffness specimen and the absorbed energy, and the numerical result showed less bending stiffness in significant numbers. It is suspected that the Kirchhoff based continuum shell SCR8 element chosen to model composite ply is not good enough to capture

actual bending stiffness because the Kirchhoff theory neglects any shear deformation, leading to a low bending stiffness prediction. A higher-order shear deformation shell element is recommended for future work to achieve a better numerical result, i.e., a better bending stiffness prediction is expected. The success of implementing a higher-order shear deformation plate bending element to handle non-linear composite plate problems has been shown in Refs. [18] and [19].

The area covered by the lines (dash line for the experimental results and solid line for the numerical result) reflects the energy absorbed and converted into permanent intra-laminar and inter-laminar damage. The experimental results showed more absorbed energy than the numerical result. The average experimental absorbed energy was 5.6 Joule; meanwhile, the numerical analysis gave an absorbed energy of 3.7 Joule. The insufficiently capable Kirchhoff based continuum shell element also influences the outcome of the predicted absorbed energy. The predicted absorbed energy reached only 67% of the test result.

5.4 Delamination Profiles

From Figures 8 and 9 below, we can see that the projected delamination profiles from the two results closely resembled each other in shape and size. The difference in area was 6.88%. The experimental result gave an average area of 896 mm^2, while the numerical result gave an area of 834 mm^2. Both shapes were close to circular, which is in agreement with the present lay-up design making the behavior of the whole plate orthotropic. Despite the problem that arises from using Kirchhoff based shell elements in predicting bending stiffness and absorbed energy, the projected delamination was in excellent agreement with the experimental result.

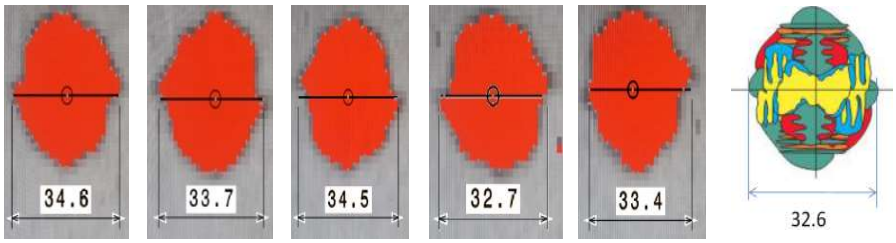

Figure 8 Projected profile of delamination for the experimental results (E1-E5) and the numerical result (FEM).

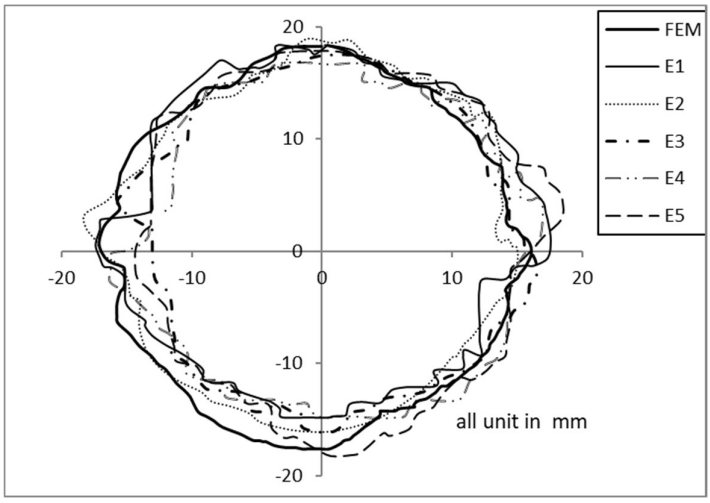

Figure 9 Comparison of projected delamination profiles: experimental (E1-E5) and numerical (FEM).

The experimental result did not reveal the depth distribution in the delamination profiles since the TTU-machine can only measure through-thickness damage. On the other hand, the numerical result provided a delamination profile for each interface layer. Figure 10 below shows the delamination profile from the numerical result for the inter-laminar's first, middle, and last cohesive layer. The largest delamination area occurred in the middle layer, i.e., the eighth cohesive layer from the top. This cohesive layer position is the closest to the neutral axis, where maximum shear stress occurs. The red color in Figure 10 indicates that the interface experienced delamination; there was no indication of delamination in the last layer.

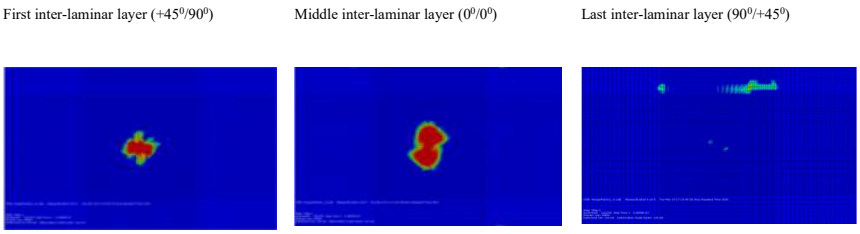

Figure 10 Delamination in first, middle, and last layer of the inter-laminar-numerical result.

5.5 Visible Surface Damage

Visible damage in the present specimen test appeared only in the form of an indention at the top surface, i.e., the impact point surface. The bottom surface showed no indication of any form of damage. The average indention size was 3.2 mm and the average depth of indention was 0.08 mm. According to Fawcett [20], an indention depth less than 0.508 mm is within the classification of BVID (barely visible impact damage). An example close-up picture of an indention is shown in Figure 11(a) below.

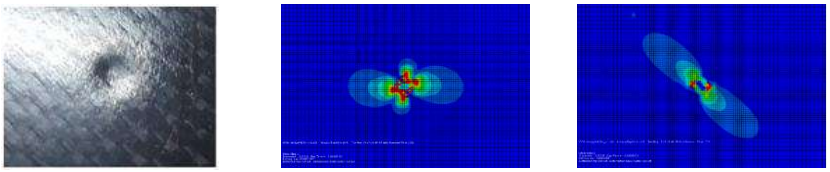

(a) (b) (c)

Figure 11 Barely visible-impact damage in the form of an indention in the top surface from the first lamina: experimental result (a), matrix compression failure, numerical result, and (b) fiber compression failure, numerical result (c).

It is noted here that the size of delamination as invisible/hidden damage was ten times larger than the size of the indention at the surface as BVID. As many references have shown, e.g., [1],[2],[3], and [4], the presence of delamination significantly reduces the compression strength of a composite plate. The numerical analysis gave only in-plane results for matrix and fiber compression failure. When the lamina are modeled by a continuum shell element there is no through-thickness failure mode, so such indentions can not be predicted. Figures 11(b) and 11(c) depict the first lamina, which failed (red aeras) under matrix and fiber compression. The last lamina showed no failure, as shown in the experimental result.

6 Conclusions

The purpose of the present work was to find the performance of the combination of a cohesive zone element and the Benzeggagh-Kenane fracture criterion in predicting the initiation and propagation of delamination. A Kirchhoff based formulation of a continuum shell element was used to model the stiffness of each lamina, and the Hashim-Rotem damage mechanism was used to predict damage in every lamina to simulate the low-velocity impact on an orthotropic uni-directional (UD) carbon/epoxy composite plate. The accuracy of predicting permanent damage after impact in the form of delamination was the main interest of the present work. Furthermore, it is noted that delamination plays a dominant

role in the compression-strength reduction of composite plates. Other minor investigation parameters considered were dynamic response, plate stiffness, visible surface damage, and absorbed energy.

The dynamic response in the form of impact force vs impact time, threshold, and peak impact force was predicted reasonably well. The minor time response delay of the numerical result compared to the experimental one is suspected due to less appropriate mass-modeling because of a lumped mass-model was used. It is more plausible to perform numerical analysis using a distributed-mass model in the future instead of a lumped-mass model. Threshold and peak force were well predicted.

The Kirchhoff based continuum shell element chosen to model the composite ply was not capable of capturing the actual bending stiffness since the Kirchhoff theory neglects any shear deformation leading to a low bending stiffness prediction. It is suspected that such incapability leads to less accurate prediction of the absorbed energy. The numerical result gave a marginal value of absorbed energy (less than 20% of the experimental value). The use of higher-order or plate elements is required in future works.

The combination of cohesive elements and the Benzeggagh-Kenane fracture criterion worked well in predicting the initiation and propagation of delamination. The resulting shape and size of the projected delamination after impact was closely similar between the experiment and the numerical results. The numerical analysis provided delamination for each interface layer. The largest delamination predicted by the numerical analysis occurred in the layer close to the neutral axis of the lamina, where maximum shear stress occurs. It is concluded that the Benzeggagh-Kenane fracture criterion also worked well in predicting mixed-mode and single-mode, i.e., shear dominant, delamination.

The Hashim-Rotem damage mechanism is adequate to predict the size of visible surface damage in the form of matrix and fiber failures by comparing it to the size of the indention in the top surface. As the lamina was modeled by a continuum shell element, no through-thickness failure mode such as indention could be predicted.

The poor performance of the Kirchhoff shell element in predicting plate stiffness and the selection of a lumped mass-model did not affect the state of the damage, such as projected delamination and surface damage size and shape predictions. Moreover, it is still an open question how such things happen.

7 Recommendations for Future Work

A recommendation for future works is (1) to replace the Kirchhoff based shell element with a higher-order shear deformation shell element, (2) to replace the lumped-mass model with a distributed-mass model, and (3) to perform more tests and numerical analyses for different impact energy values, lay-up configurations, i.e., different stacking sequences and fiber orientations.

Acknowledgement

The present work was fully funded by Institut Teknologi Bandung through P3MI (*Program Penelitian Pengabdian Masyarakat dan Inovasi*), fiscal year 2020. Testing and specimen preparation were performed at PT Dirgantara Indonesia.

References

[1] Sanchez-Saez, S., Barbero, E., Zaera, R. & Navarro, C., *Compression after Impact of Thin Laminates Composite Laminates*, Composites Science and Technology, **65**(13), pp. 1911-1919, June 2005.

[2] Rivallant, S., Bouvet, C. & Hongkarnjakul, N., *Failure Analysis of CFRP Laminates Subjected to Compression after Impact: FE Simulation Using Discrete Interface Elements*, Composites: Part A., **55**, pp. 83-93, Dec. 2013.

[3] Rivallant, S., Bouvet, C. & Broll, B., *Experimental Analysis of CFRP Laminates Subjected to Compression after Impact: The Role of Impact-Induced Cracks in Failure*, Composite Structures, **111**(1), pp. 147-157, May 2014.

[4] Gonzalez, E.V., Maimi, P., Camanho, P.P., Turon, A. & Mayugo, J.A., *Simulation of Drop-Weight Impact and Compression after Impact Tests on Composite Laminates*, Composite Structures, **11**, pp. 3364-3378, Nov. 2012.

[5] Gonzalez, E.V., Maimi, P., Camanho, C.S. & Blanco, N., *Effects of Ply Clustering in Laminated Composites Plates Under Low-Velocity Impact Loadin*g, Composites Science and Technology, **71**(6), pp. 805-817, 2011.

[6] Bouvet, C. & Rivallant, S., *Low-Velocity Impact Modeling in Composite Laminates Capturing Permanent Indentation*, Composites Science and Technology, **72**(16), pp. 1977-1988, Nov. 2012.

[7] ASTM D7136, *Standard Test Method for Measuring the Damage Resistance of a Fiber-Reinforced Polymer Matrix Composite to a Drop Weight Impact Event*, 2020.

[8] Allen, J.F., *Composite Airframe Damage Tolerance and Service Experience*, Damage Tolerance Workshop, July 19-21, 2006. http://www.niar.wichita.edu/chicagoworkshop/Chicago.

[9] Suada, M.G., Syamsudin, H. & Simanjorang, H.C., *Finite Element Analysis of Composite Plate Subject to Low-Velocity Impact and Compression after Impact*, The 10th AUN/SEED-Net RC MEManuE, 7th-8th November 2019.
[10] Song, K., Dávila, C.G. & Rose, C.A., *Guidelines and Parameter Selection for the Simulation of Progressive Delamination*, Proceedings of 2008 Abaqus Users' Conference, 2008.
[11] *ABAQUS 6.13 Theoretical Manual*, Providence (RI, USA): Dassault Systemes Simulia Corp., 2011
[12] Aldyandra, *Comparison between Cohesive Zone and 3D Brittle Fracture Models for Simulating Composite Laminate Delamination in Low-Velocity Impact*, Master Thesis, Aeronautic Department, Institut Teknologi Bandung, Indonesia, 2015.
[13] Zhang, X., Hounslow, L. & Grassi, M., *Improvement of Low- Velocity Impact and Compression- After Impact Performance by Z- Fiber Pinning*, Composites Science and Technology, **66**(15), pp. 2785-2794, Dec. 2006.
[14] *ABAQUS 6.13 User's Manual,* Providence (RI, USA): Dassault Systems Simulia Corp., 2011.
[15] Richardson, M.O.W. & Wisheart, M.J., *Review of Low – Velocity Impact Properties of Composite Materials*, Composites Part A: Applied Science and Manufacturing, **27**(12), pp. 1123-1131, 1996.
[16] Hashin, Z. & Rotem, A., *A Fatigue Criterion for Fiber-reinforced Materials*, J. Composite Materials, **7**, pp. 448-464, 1973.
[17] Benzeggagh, M.L. & Kenane, M., *Measurement of Mixed-mode Delamination Fracture Toughness of Unidirectional Glass/Epoxy Composite with Mixed-Mode Bending Apparatus*, Composite Science and Technology, **56**, pp. 439-449,1996.
[18] Al-Furjan, M.S.H., Dehini, R., Paknahad, M., Habibi, M. & Sarfarpour, H., *On the Nonlinear Dynamics of the Multi-Scale Hybrid Nanocomposite-Reinforced Annular Plate Under Hygro-thermal Environment*, Archives of Civil and Mechanical Eng., **21**(1), 4, March 2021.
[19] Al-Furjan, M.S.H., Samimi-Sohrforozani, E., Habibi, M., Jung, D.W. & Safarpour, H., *Vibrational Characteristics of a Higher-Order Laminated Composite Viscoelastic Annular Microplate via Modified Couple Stress Theory*, Composite Structures, **257**, 113152, 2021.
[20] Fawcett, A.J., *Composite Airframe Damage Tolerance and Service Experience*, Damage Tolerance Workshop, July 19-21, 2006. http://www.niar.wichita.edu/chicagoworkshop/Chicago.